Spectrochimica Acta Part A: Molecular and Biomolecular Spectroscopy 305 (2024) 123521

Contents lists available at ScienceDirect

Spectrochimica Acta Part A:
Molecular and Biomolecular Spectroscopy

journal homepage: www.journals.elsevier.com/spectrochimica-acta-part-a-molecular-and-biomolecular-spectroscopy

Discrimination of resected glioma tissues using surface enhanced Raman spectroscopy and Au@ZrO_2 plasmonic nanosensor

Vaclav Ranc [a,*], Ondrej Pavlacka [b], Ondrej Kalita [c,d], Miroslav Vaverka [c]

[a] Institute of Molecular and Translational Medicine, Faculty of Medicine and Dentistry, Palacký University and Faculty Hospital Olomouc, Hněvotínská 5, 775 15, Olomouc, Czech Republic
[b] Department of Mathematical Analysis and Applications of Mathematics, Faculty of Science, Palacký, University Olomouc, 17. Listopadu 12, Olomouc, Czech Republic
[c] Department of Neurosurgery, Faculty Hospital Olomouc, I.P. Pavlova 6, 775 20, Olomouc, Czechia
[d] Department of Health Care Science, Faculty of Humanities, T. Bata University in Zlín, Štefanikova 5670, 760 01 Zlín, Czechia

HIGHLIGHTS

- Gliomas present one of the most prevalent malignant tumors related to the central nervous system.
- A new method for the analysis of brain tissue was developed.
- The method is based on Au@ZrO_2 plasmonic nanosensor.
- This method allows them to distinguish between central and peripheral parts of the tumor tissue.

GRAPHICAL ABSTRACT

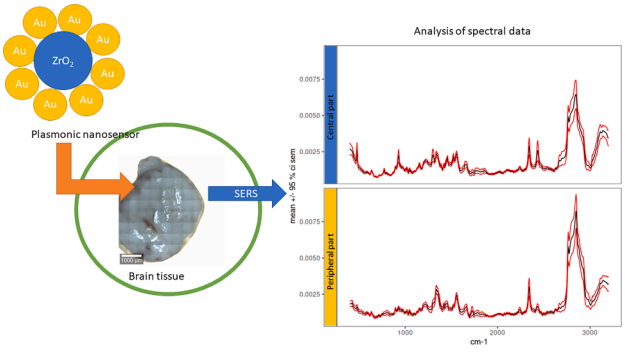

ARTICLE INFO

Keywords:
Raman spectroscopy
Gliomas
Nanomaterials
SERS
ZrO_2
Au nanospheres

ABSTRACT

Gliomas present one of the most prevalent malignant tumors related to the central nervous system. Surgical extraction is still a preferred route for glioma treatment. Nonetheless, neurosurgeons still have a considerable challenge to detect actual margins of the targeted glioma intraoperatively and correctly because of its great natural infiltration. Here we evaluated the possibility of using surface-enhanced Raman spectroscopy to analyze freshly resected brain tissues. The developed method is based on the application of Au@ZrO_2 nanosensor. The plasmonic properties of the sensor were first tested on the analysis of Rhodamine 6G, where concentrations down to 10^{-7} mol/L can be successfully detected. We also compared the performance of the nanosensor with silver plasmonic nanoparticles, where similar results were obtained regarding the reduction of the fluorescence background and enhancement of the intensity of the measured analytical signal. However, application of silver nanospheres led to increased variations in spectral data due to its probable aggregation. Applied ZrO2@Au nanosensor thus dramatically lowers the fluorescence present in the Raman data, and considerably improves the quality of the measured signal. The developed method allows for rapid discrimination between the glioma's periphery and central parts, which could serve as a steppingstone toward highly precise neurosurgery.

* Corresponding author.

https://doi.org/10.1016/j.saa.2023.123521
Received 4 April 2023; Received in revised form 6 October 2023; Accepted 11 October 2023
Available online 14 October 2023

1. Introduction

Gliomas of astrocytic, oligodendroglial, and ependymal origin represent more than 70 % of all intracranial tumors, marking them as one of the most prevalent malignant tumors related to the central nervous system. The total occurrence is six newly diagnosed patients per 100,000 each year, which leads to a considerable mental and, so also, economic impact on our society. [1] In the last years, primary malignant brain tumor incidence has been increasing, with an annual growth rate of more than 1 %. Gliomas preferably affect the elderly and middle-aged population, as recent reports suggest. [2–3] According to the World Health Organization, gliomas are classified into four grades. [4] The first two grades are considered low-grade gliomas, and the last two are labeled as advanced gliomas, respectively. Despite the recent advances in therapeutic strategies, which also include new substances for chemotherapy and new procedures in radio-chemotherapy, and intelligent approaches in the operative resection using MRI (Magnetic Resonance Imaging), fluorescence labels, electrostimulation, or confocal microscopy, the prognosis continues to be unsatisfactory, with a median for the survival of newly diagnosed gliomas around 41 weeks (about nine and a half months).[5] Developing a more advanced strategy for precise detection of low-grade gliomas is thus demanding. Diagnosis and consecutive classification of gliomas rely on tumor histopathologic properties, which supply only limited information on the response to a follow-up therapy or further patient's prognosis. [6] The decision about the treatment of patients diagnosed with glioma is usually based on the analysis of tissue, including the evaluation of the presence of selected molecular markers, which are relevant for the diagnosis. Upfront surgery is thus commonly performed for both diagnostic and therapeutic purposes. Based on 2016 WHO classification and cIMPACT-NOW recommendations, respectively, the following molecular biomarkers play vital roles in the categorization of diffuse gliomas in adults: histone H3.3 G34R/V mutation, histone H3 K27M mutation, IDH mutation, 1p/19q co-deletion, TERT promoter mutation, amplification of the EGFR gene, a combination of the Chromosome 7 gain and chromosome 10 loss, and homozygous deletions on 9p21 involving the CDKN2A and CDKN2B gene loci. [7] The use of techniques of molecular spectroscopy, particularly Raman spectroscopy in diagnosing gliomas has been fruitful and led to valuable research data. Raman spectroscopy has been used in both scenarios, statistical analysis of data acquired from the whole brain tissues and analysis of molecular markers, including nucleic acids and proteins in various clinical samples. Works presented by Uckermann [8] and Sciortino [9] aimed at analyzing IDH1 mutation by means of Raman spectroscopy. Uckermann reported an increased signal of DNA and decreased signal of lipids in samples, where a mutation of IDH1 was reported next to alterations in protein band signatures. Sciortino reported similar data on detecting IDH1 mutations related to altered levels of lipids, collagen, DNA, cholesterol, and phospholipids. Zhou spectrally analyzed brain tissue samples to recognize new molecular markers, and concentrations of ATM and lactic acids were reported in this work as potential markers. [10] Livermore published a paper covering gliomas' fast and genetic classification. [11] Research papers aimed at utilizing Raman spectroscopy in the analysis of processed or bare brain tissues stand for most works involving this spectroscopy in the detection of gliomas. [12–18] Published data uses bare tissues and processed tissue fluids, and some involve application of surface enhanced Raman scattering. [19–22] However, there is still a considerable scientific challenge in developing Raman spectroscopy-based approaches utilizing new plasmonic nanomaterials, which would utilize plasmonic nanocomposites to minimize the effect of fluorescence and amplify the measured effect of Raman signal to improve the method sensitivity and selectivity.

Here we have developed a new method for analyzing intact brain tissue using a surface-enhanced Raman spectroscopy. The technique uses a plasmonic Au@ZrO_2 nanocomposite to increase the information level of the measured spectral data. According to our knowledge, this nanomaterial is used in this scenario for the first time. Nanomaterials allow amplifying the analytical signal and minimize the adverse effects of sample fluorescence. [23–25] Here developed method allows discrimination between the central part of the high-grade tumor tissue and the surrounding peripheral tissues without any need for a complex sample processing. The method potential was evaluated on freshly resected samples obtained during neurosurgery. For each patient, two samples were collected and labeled P and C. Sample P stands for periphery and was resected from the peripheral part of the tumorous tissue. C stands for the central part of the tumorous tissue with higher variability given by factors including phenotype of the tumor, presence of necrosis, presence of blood.

2. Experimental

2.1. Chemicals

The LC-MS Grade water, citric acid (p.a.), and $HAuCl_4$ (p.a.) were obtained from Merck (U.S.A.). 5-Ethynyl- 2′-deoxycytidine (p.a., EdC), cysteamine (p.a.) and N-hydroxysuccinimide (p.a.) were brought from Merck (U.S.A.), ZrO_2 nanoparticles were purchased from Merck (U.S.A.). CaF_2 substrates for Raman measurements were purchased from Crystran (U.K.).

2.2. Resection of the tissues, preparation of samples

All patients underwent a standard glioma resection. The maximal, but safe tumor removal was considered a purpose of this procedure. Along with the surgeries were performed sampling in the different sites to cover glioma tissues heterogeneity. Part of the obtained biopsy specimen was fixed in formalin and embedded in paraffin. By this way processed tumor tissue was stained with hematoxylinphloxin-saffron and histologically analyzed. The second part of biopsy specimen was stored in liquid nitrogen (- 196 °C) as a fresh-frozen sample.

2.3. Synthesis of Au nanoparticles

The gold nanospheres were synthesized according to a modified procedure earlier described by Turkevich, based on a reduction of an aqueous solution of chloroauric acid ($HAuCl_4$) by a sodium citrate. Briefly, 150 μL of 1 % chloroauric aqueous solution was heated up to the boiling point, and consequently, 8 mL of 1 % sodium citrate was slowly added under constant stirring at 300 RPM using a magnetic stirrer.

2.4. Synthesis of Au@ZrO_2 plasmonic nanoclusters

The Au@ZrO_2 nanoclusters were synthesized as follows. First, 5 mL of a stocked suspension of ZrO_2 nanoparticles was mixed with 0.5 mL of 1 mM EDC and 0.5 mM NHS and shaken for three hours at room temperature. Then, 1 mL of 1 mM aqueous solution of cysteamine was added, and the mixture was shaken overnight at room temperature. Finally, 0.5 mL of a previously prepared suspension of Au nanoparticles was added, and the system was shaken overnight at room temperature. The excess of EDC and cysteamine were removed using dialysis through a 10 nm pore-sized cellulose membrane (Merck, U.S.A.).

2.5. Characterization of Au@ZrO2 nanocomposite

Firstly, the as-prepared nanomaterial was characterized using transmission electron microscope LVEM5 (Delong., Brno. Czech Republic) using 3 kV acceleration voltage to obtain information on the chemical composition of the prepared nanoclusters. Next, Raman microscopy (Witec alpha 300R+, Witec, Germany) was applied in the characterization of the nanomaterial. Laser working at 532 nm and power of 1 mW on sample was used with 1 s exposition time. In total 32 spectra were averaged to obtain one data point. For the evaluation of the

plasmonic properties, aqueous samples holding the Au@ZrO_2 and Rhodamine 6G at defined concentration levels (range 0 – 1x10^{-3} mol/L, according to description in the Results and discussion section) were deposited in 2 μL droplets on a surface of CaF_2 microscopy glass, let dry and measured in the center of the deposited sample. Spectral background in the raw data was corrected by a subtraction of the polynomial function (degree = 5), data were smoothed using Savitsky-Golay algorithm.

2.6. Preparation of tissues for spectral measurement

Two samples were obtained during the surgery for each patent: sample C (central part of the cancerous tissue) and P (peripheral part of the cancerous tissue). The position of the sample extraction was based a) on 3D MRI navigation, where the respective MRI data were obtained before the surgery and correlated to the position of the patient's head during the surgery and b) on the presence of fluorescence of the applied ALA (5-Aminolevulinic acid) probe. ALA fluorescent probe can be considered as a golden standard for a discrimination between healthy and cancerous tissues during the neurosurgery. Brain tissues (P and C parts separately) were washed with LC-Grade water, resected to size of approximately 2 cubic millimeters, and rinsed in the suspension of Au@ZrO_2 for 20 min. Samples were then removed and deposited on the CaF_2 substrate. Next, Raman spectra from ten randomly selected spots were collected using the parameters described in section 2.7 on both samples.

2.7. Analysis of the tissues using Raman spectroscopy

Raman spectrometer was used for spectral characterization of the samples. The Raman system was equipped with a green laser working at 532 nm, running at 1 mW power on the sample. The exposition was set to 1 s; spectra are averages of 28 micro-scans. Each sample was deposited on CaF_2 microscopy glass (Crystran, U.K.), and measured on ten randomly selected spots. This gives in total 560 Raman micro-scans obtained for one patient, 280 for sample C, and P, respectively. Raman spectra were averaged (28 micro-scans per measured spot into one Raman spectrum), sorted according to patient ID and measured sample spot and extreme values were removed based on constructed box plots, where two spectra were based on the signal intensity identified as extreme. Further analysis uncovered presence of abundant signals of the carbon-related bands present at 1290 and 1600 cm-1 (D and G bands), which indicate a burning process. These two spectra were removed from the data set. The statistical analysis is based on the analysis of 178 spectra of 9 patients, 91C samples, and 87P samples. Rstudio (RStudio, Boston, U.S.A.) was chosen for data processing in the ChemoSpec package [26].

2.8. Computational analysis

SERS spectra were processed using MATLAB R2016b (MathWorks, Inc., USA). First, cosmic rays (spikes) were removed by Whitaker and Hayes, a modified Z-score based approach [27]. Then, for smoothing and background substruction, iterative automatic baseline correction method described in [28] was applied with following parameters: Window size 7 points, threshold 0.000021, parameters were determined visually. Finally, all data points of each spectrum were mean centered.

3. Results and discussion

3.1. Method development

First, we characterized the prepared Au@ZrO_2 nanoclusters using transmission electron microscopy to obtain data on their size, distribution, and morphology. The representative micrograph can be found in Fig. 1A. It is shown that the prepared nanomaterial is formed from interconnected structures of Au and ZrO_2 nanospheres organized in heterogeneous clusters. The average size of the Au nanoparticles is 30 nm, and the respective size of ZrO_2 nanospheres is 10 nm (based on averaging across 100 identified particles). Next, we characterized the

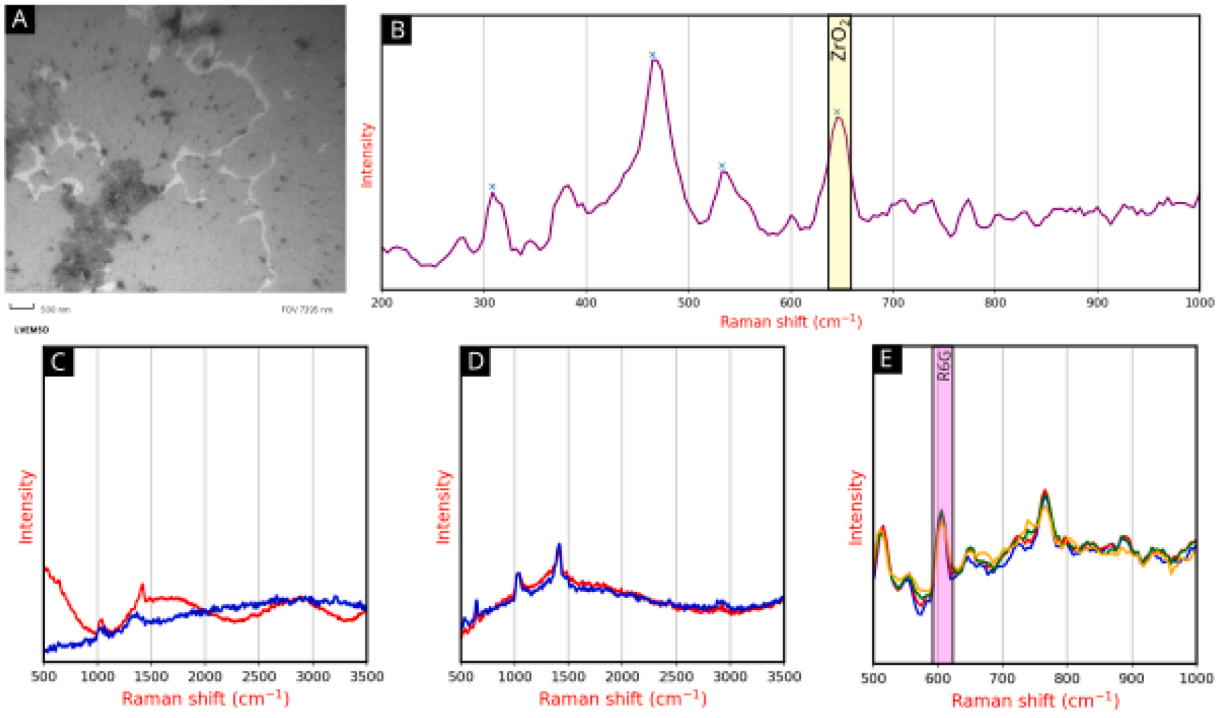

Fig. 1. A) Micrograph image of the prepared nanomaterial, B) Raman spectrum of the substrate, C) SERS spectra of R6G at 1x10^{-6} mol/L, obtained by the application of gold (blue) and ZrO_2 (red) nanomaterials per se, D) SERS spectra of R6G at 1x10^{-6} mol/L, obtained by the application of Au@ZrO_2 nanomaterial, E) repeated SERS measurements of R6G at a concentration level of 1x10^{-6} mol/L using Au@ZrO_2 nanosensor.

nanoclusters using Raman microscopy. The resulting representative Raman spectrum is shown in Fig. 1B. The Raman spectrum has a broad spectral band at 640 cm^{-1}, characteristic of ZrO_2, as previously shown by Purohir [29]. Two spectral bands between 280 and 320 cm-1 cans be seen as Au-S breathing vibrations according to Varnholt et al. [30], indicating cysteamine molecules on the surface of gold nanoclusters.

Next, plasmonic properties and the ability of the nanoclusters to serve as a SERS substrate were evaluated in the analysis of Rhodamine 6 g. First, plasmonic properties of both Au and ZrO_2 nanoparticles were evaluated separately on the analysis of Rhodamine 6G at a concentration level of $1x10^{-5}$ mol/L. Raman spectra are shown in Fig. 1C, where almost no SERS effect was seen. The reason can be found in a not perfectly suitable position of the plasmon frequency of the used nanostructures. Follow-up measurements of Rhodamine 6G using an Au@ZrO_2 nanosensor can be found in Fig. 1D and 1E. Fig. 1D shows Raman spectra of Rhodamine 6G measured at a concentration level of $1x10^{-6}$ mol/L. Spectra contain characteristic bands for this compound, including spectral band at 611 cm^{-1} (C–C–C ring in-plane bending), spectral band at 1127 cm^{-1} (C–H in-plane bending) or spectral band at 1276 cm^{-1} (C-O-C stretching). Fig. 1E contains five Raman spectra obtained in the repeated study of R6G at a concentration level of $1x10^{-6}$ mol/L. The resulting spectral data are fully comparable. Next, concentration levels from $1x10^{-4}$ to $1x10^{-7}$ mol/L of R6G were measured to evaluate the effect of various concentrations. In particular, we selected levels 10^{-7}, $10^{-6,}$ 10^{-5} and 10^{-4} mol/L. The SERS signal obtained by the measurement of R6G at the concentration level of 10^{-6} increased considerably, when compared to data obtained at 10^{-7} mol/L (Fig. 2A and 2B). The same trend was observed between levels 10^{-6} and 10^{-5} mol/L. However, almost no increase in the signal intensity was observed between measurement of concentrations 10^{-5} and 10^{-4} mol/L. Based on this information, it could be stated that the system has no capacity left for the binding of additional molecules of analyte.

The developed nanosensor was evaluated in the analysis of the freshly resected brain tissues. The testing brain tissue of the central part of the glioma was washed with water and then rinsed for 20 min in the suspension of the prepared nanocomposite. Next, the sample was rinsed with water and deposited between two microscopy glasses for spectral analysis. Microscopy images of one of the analyzed pieces can be seen in Fig. 2C. Ten spots were measured to obtain one representative spectrum, shown in Fig. 2D in red. The same procedure was also performed without adding the nanoclusters, with the result also shown in Fig. 2D in blue color. The blue spectrum obtained without SERS is highly influenced by fluorescence. We can state that the addition of plasmonic nanoclusters improved the quality of spectral data. Follow up measurements of tissues, namely central and peripheral parts of gliomas, were performed using synthesized plasmonic nanosensors according to the previously described procedure.

To further evaluate the application potential of the Au@ZrO_2 nanosensor, we performed a comparative study with the silver nanoparticles, which are commonly used in SERS applications. Silver nanomaterial was characterized using transmission electron microscopy with results shown in Fig. S1A. It can be seen that the synthesized material consists of silver nanospheres with a diameter of approximately 30 nm. The comparison was consequently based on the analysis of ten spots on the P sample using both nanomaterials. Obtained results are shown in Fig. S1B. The average SERS signal is shown as a black trace, red lines stand for ± quartiles. The reduction of the fluorescence background and increase of the level of analytical signal obtained from the use of silver plasmonic nanomaterial is comparable to data obtained from the application of Au@ZrO_2 nanosensor. However, the spectral variability is considerably higher for silver nanoparticles. This phenomenon can be caused by a decreased stability of silver nanospheres in biological matrixes, which tend to aggregate into large clusters. This has a considerable impact on the present plasmon frequency as well as on the ability to perform SERS experiments. Further experiments were thus performed using solely Au@ZrO_2 nanosensors.

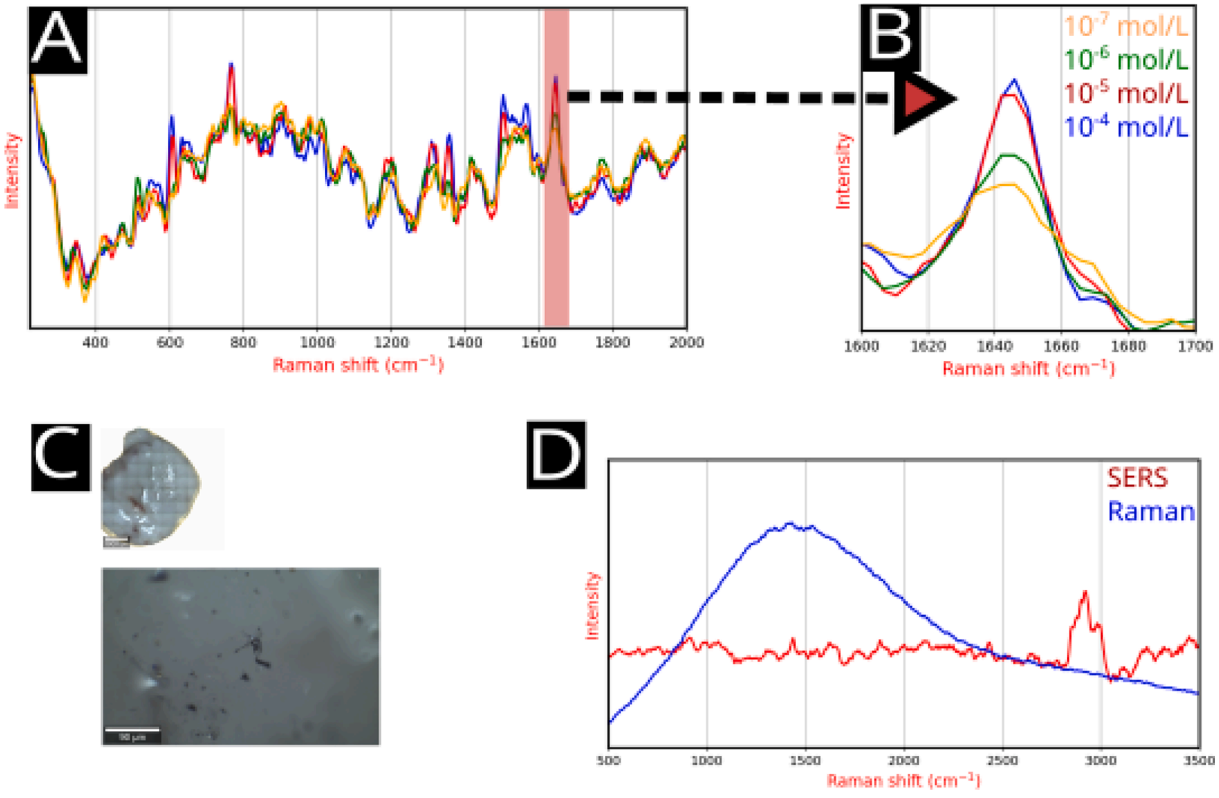

Fig. 2. A) SERS spectra obtained by the analysis of R6G at a concentration range from $1x10^{-7}$ to $1x10^{-4}$ mol/L, B detail of Fig. 2A, C: microscopy images of the resected and treated brain tissue, D: representative Raman (in blue color) and SERS (in red color) spectrum of the brain tissue.

3.2. Analysis of samples of gliomas

We analyzed SERS spectra from 9 patients. For each patient, about half the samples were from the central part of a glioma (C samples) and the rest were from the periphery (P samples). In total, we dealt with 178 SERS spectra, 91 from C samples and 87 from P samples. The analyzed spectral range was set from 500 to 1800 cm^{-1}, dimension of each single spectrum was 1 × 311 data points. The measured SERS spectra were processed as described in Section 2.8. An example of SERS spectra from four different patients is shown in Fig. 3. Even though the variability of the spectral data between patients is relatively high; we were able to find common spectral bands between samples of one patient (C and P), including amide I (1650 cm-1), amide II (1550 cm-1) or bands of glutathione (around 1050 cm-1) and trends in these bands between patients. Spectra variation between data for one biological sample is acceptable, as it can be seen in Fig. 3 and figure S2, which allowed to observe significant spectral differences between P and C samples and analyze the differences.

It can be easily seen in Fig. 3. that the behavior of SERS spectra varies between selected four patients. This is true also for SERS spectra for the remaining five patients (SERS spectra of all nine patients are shown in figure S2). Hence, it is not reasonable to sample-pool SERS spectra of various patients and look for a general marker standing for either central or peripheral parts. However, if we consider only samples obtained from a single patient, then the SERS spectra from both kinds of samples are mostly distinguishable at first sight. We thus developed the following discriminant analysis, which is easily applicable to each patient separately.

For a given patient, the central part of a glioma is clearly given by C samples. Our aim is to distinguish peripheral tissue surrounding the glioma. Let us denote the i-th SERS spectrum by $x^i = (x^i_1, \cdots, x^i_{311})$, where x^i_j means Raman intensity at j-th Raman shift. We can describe the typical behavior of SERS spectra from the central part by the mean SERS spectrum $m_C = (m_1, \cdots, m_{311})$ of C samples from the patient, and by the vector $s_C = (s_1, \cdots, s_{311})$ of standard deviations of SERS spectra from C samples in each measured Raman shift (we smoothed s_C with a moving average MA(3) for removing possible zeroes and reducing noise). From s_C, it can be seen the Raman shifts, in which the SERS spectra of the central part differ from each other, and where they have similar behavior. Then, for each SERS spectrum x^i, the coefficients of standardized differences from m_C in each measured Raman shift are given as a vector $k^i = \left(k^i_1, \cdots, k^i_{311}\right)$, where $k^i_j = \frac{|x^i_j - m_j|}{s_j}$, $j = 1, \ldots, 311$. The behavior of these differences in the case of selected four patients are shown in Fig. 4A (the behavior of differences of all nine patients are shown in figure S3). In theory, it is possible that some k values at wavenumbers near 0 Raman intensities are very large for either P or C samples (this occurs in our data only in several C samples). Therefore, we set $k^i_j = 0$, if both $x^i_j < 0.1$ and $m_j < 0.1$, to ensure that in the following procedure, the meaningful values of k come from characteristic Raman peaks only. In Fig. 4B, we show two box plots of maximal coefficients $k^i_{max} = \max_{j=1,\ldots,311}\left\{k^i_j\right\}$ from all C samples and from all P samples over all patients, as shown in the Table 1. In figure S4, it is shown the histogram of wavenumbers in which the k_{max} values for C and P samples are located.

It can be easily seen from Fig. 4B that the maximal coefficients k^i_{max} are in case of P samples mostly considerably greater than in case of C samples. Hence, we can distinguish P samples from C samples by the following simple rule: For some threshold $T > 0$, if $k^i_{max} < T$, then the i-th SERS spectrum represents a C sample, otherwise, the tissue is classified as a P sample. The threshold T stands as the trade-off between precision $\mathrm{Pr} = \frac{trueP}{(trueP + falseP)}$ and recall $\mathrm{Re} = \frac{trueP}{(trueP + falseC)}$. The dependence of these characteristics on the value of T is shown in Fig. 5A-B. The overall performance of the classification can be expressed by F_1 score given as a harmonic mean of Pr and Re, i.e., $F_1 = \frac{2PrRe}{Pr+Re}$. In Fig. 5C, we can see that the best performance is obtained for T between 4.3 and 4.6. To validate this technique, we applied a cross-validation in which we gradually excluded all patients one by one from data set and set the T in such a way

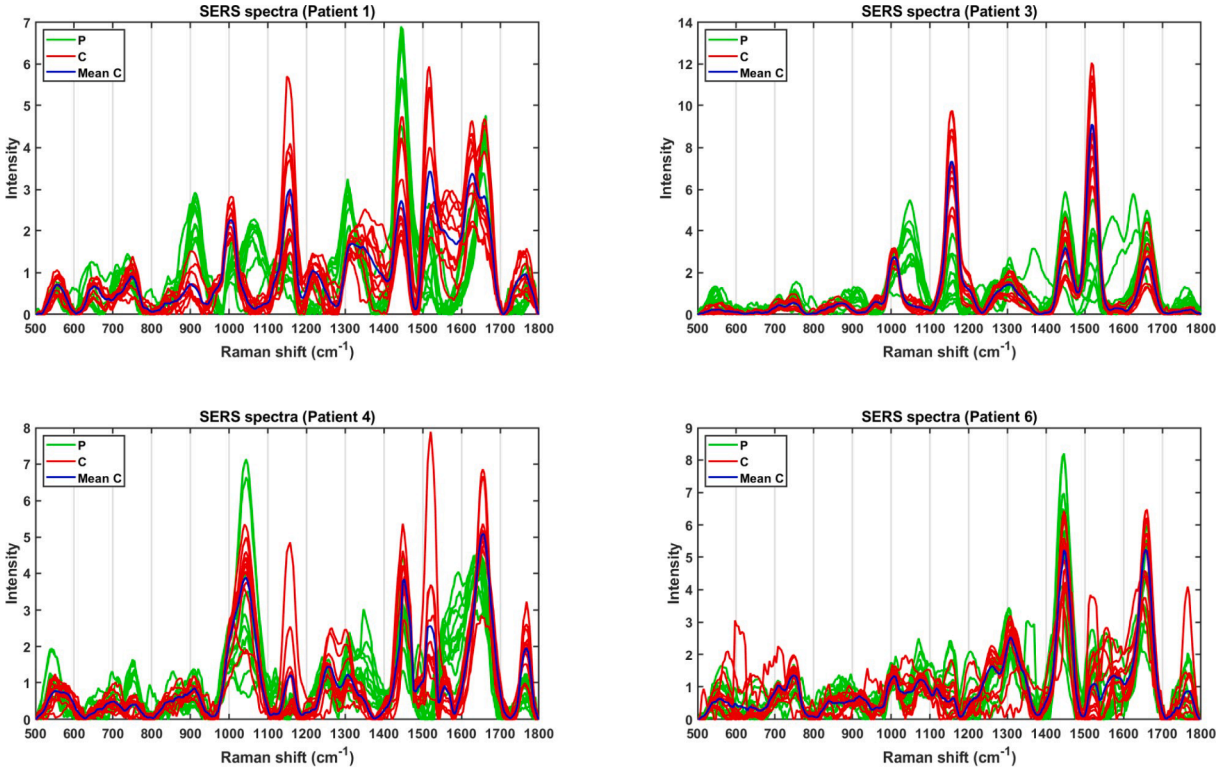

Fig. 3. Processed SERS spectra of the brain tissues of selected four patients. Green spectra – samples from the periphery of a glioma. Red spectra – samples from the central part of a glioma. Blue spectrum – mean of spectra from the central part of a glioma.

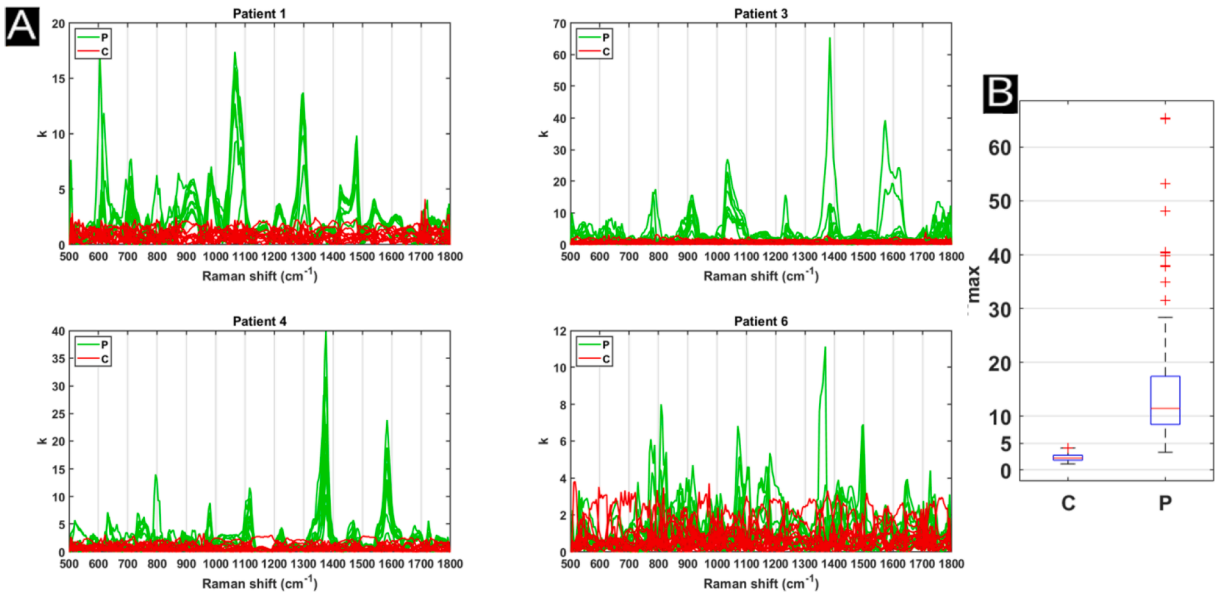

Fig. 4. A) Behavior of standardized differences k^i of selected four patients. Green lines – samples from periphery of glioma. Red lines – samples from central part of glioma. B) Box plots of maxima of coefficients k from samples (C = samples from central parts of gliomas, P = samples from peripheries of gliomas).

Table 1
Performance of the proposed discriminant technique.

Patient	$k^i_{max} < 4.5$/C	$k^i_{max} \geq 4.5$/P	$k^i_{max} < 4.5$/P
1	10/10	10/10	0/10
2	5/5	5/5	0/5
3	11/11	10/10	0/10
4	11/11	11/11	0/11
5	12/12	10/10	0/10
6	12/12	11/11	0/11
7	10/10	10/10	0/10
8	10/10	9/10	1/10
9	10/10	10/10	0/10
Overall	91/91	86/87	1/87

that F_1 score for remaining eight patients is maximized. The range of T varies between 4.2 and 4.8, thus, the midpoint $T = 4.5$ is considered further. For this threshold, only one P sample would have its $k^i_{max} < T$, and all C samples would be classified correctly (see table 1). The one SERS spectrum from P sample that is classified as C sample has very similar behavior as the spectra from C samples of patient 8. It can be caused by the fact that in this sample, the tumor tissue is present also in the peripheral tissue region.

Interestingly, one of the variations seen in the measured Raman spectra (see Fig. 4A, or S4, respectively) is the presence of the spectral band at 1040 cm^{-1}, which could be interpreted as a presence of glutathione, which is often associated with the altered metabolism in cancerous cells. [31].

4. Conclusions

We showed that $Au@ZrO_2$ nanocomposite can amplify Raman signal using SERS on the example of model compound, Rhodamine 6G. The developed method allowed detecting this molecule at the concentration $1x10^{-7}$ mol/L. Next, the prepared nanocomposite was used in the analysis of central and peripheral samples of gliomas and compared to data obtained using silver nanospheres applied in the same experimental arrangement. In total, 178 averaged spectra were obtained and processed. The developed method, based on computational processing, suggests a possibility to discriminate between the central part of gliomas and the peripheral tissue surrounding the tumor. The discrimination is based on the k_{max} factor with a threshold set to a value of 4.5 which maximizes F_1 score. In total, 91 out of 91 SERS spectra originated from the central part of the tumor meet this criterium. Importantly, also 86 out of 87 SERS spectra obtained at the peripheral part are classified correctly, which suggests that 1 spectrum has a high similarity to spectra obtained from the central part. This assignment could be potentially caused by the presence of a higher number of tumor cells in this sample.

Supplementary materials:

The following supplementary information can be downloaded: Method for the synthesis of silver nanospheres, figure S1: A: micrograph of the ag nanospheres, B: SERS spectra of the peripheral tissue obtained

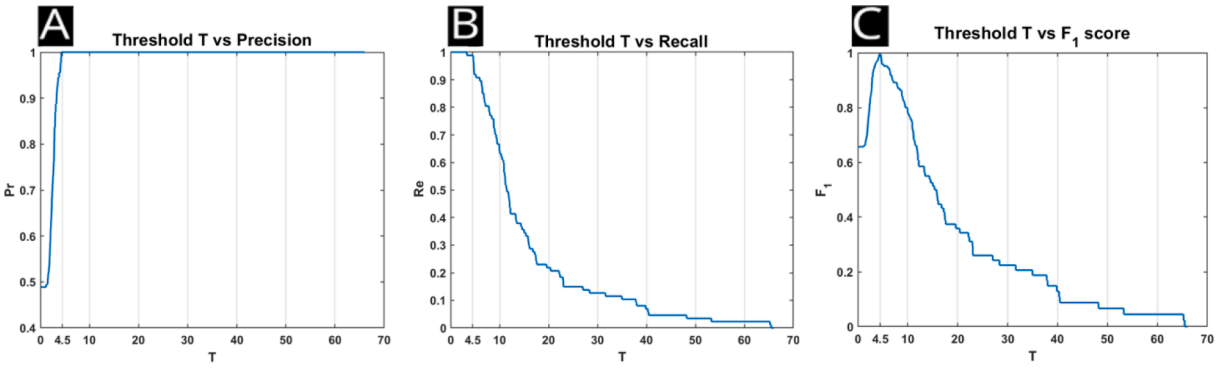

Fig. 5. A) Dependence of Precision on the threshold T. B) Dependence of Recall on the threshold T. C) Dependence of F_1 on the threshold T.

by the analysis using Ag nanospheres and Au@ZrO_2 nanocomposite., figure S2: Processed SERS spectra of the brain tissues of all nine patients. Green spectra – samples from the periphery of a glioma. Red spectra – samples from the central part of a glioma. Blue spectrum – mean of spectra from the central part of a glioma, and Fig S3: *Behavior of standardized differences* k^i *of all nine patients*. Green lines – samples from periphery of glioma. Red lines – samples from central part of glioma. Fig S4: Histogram of location of coefficients k_{max}. Green bars – samples from periphery of glioma. Red bars – samples from the central part of glioma.

CRediT authorship contribution statement

Vaclav Ranc: Conceptualization, Methodology, Data curation, Writing – original draft. **Ondrej Pavlacka:** Data curation, Writing – original draft, Formal analysis, Validation. **Ondrej Kalita:** Writing – review & editing, Conceptualization. **Miroslav Vaverka:** Supervision, Funding acquisition, Writing – review & editing.

Declaration of Competing Interest

The authors declare that they have no known competing financial interests or personal relationships that could have appeared to influence the work reported in this paper.

Data availability

Data will be made available on request.

Acknowledgment

The work was supported by the Ministry of Health of the Czech Republic, grant nr. NV19-04-00281. Authors also thank NANO4TARMED consortium (H2020 WIDESPREAD-2020-5, project number 952063). The work was further supported by the MEYS CR (Large RI Project LM2018129 Czech-BioImaging) and by the project National Institute for Cancer Research (Programme EXCELES, ID Project No. LX22NPO5102)—Funded by the European Union—Next Generation EU.

Appendix A. Supplementary material

Supplementary material to this article can be found online at https://doi.org/10.1016/j.saa.2023.123521.

References

[1] H. Ohgaki, P. Kleihues, Epidemiology and etiology of gliomas, Acta Neuropathologica 109 (2005), https://doi.org/10.1007/s00401-005-0991-y.
[2] H. Ohgaki, P. Kleihues, Population-based studies on incidence, survival rates, and genetic alterations in astrocytic and oligodendroglial gliomas, Journal of Neuropathology and Experimental Neurology 64 (2005), https://doi.org/10.1093/jnen/64.6.479.
[3] D.J. Cote, Q.T. Ostrom, H. Gittleman, K.R. Duncan, T.S. CreveCoeur, C. Kruchko, T. R. Smith, M.J. Stampfer, J.S. Barnholtz-Sloan, Glioma incidence and survival variations by county-level socioeconomic measures, Cancer 125 (2019), https://doi.org/10.1002/cncr.32328.
[4] P. Kleihues, F. Soylemezoglu, B. Schäuble, B.W. Scheithauer, P.C. Burger, Histopathology, classification, and grading of gliomas, Glia 15 (1995), https://doi.org/10.1002/glia.440150303.
[5] A. Perry, P. Wesseling, Histologic classification of gliomas, Handbook of Clinical Neurology (2016), https://doi.org/10.1016/B978-0-12-802997-8.00005-0.
[6] M. Nuño, K. Birch, D. Mukherjee, J.M. Sarmiento, K.L. Black, C.G. Patil, Survival and prognostic factors of anaplastic gliomas, Neurosurgery 73 (2013), https://doi.org/10.1227/01.neu.0000431477.02408.5e.
[7] E.R. Laws, I.F. Parney, W. Huang, F. Anderson, A.M. Morris, A. Asher, K.O. Lillehei, M. Bernstein, H. Brem, A. Sloan, M.S. Berger, S. Chang, Survival following surgery and prognostic factors for recently diagnosed malignant glioma: Data from the glioma outcomes project, Journal of Neurosurgery 99 (2003), https://doi.org/10.3171/jns.2003.99.3.0467.
[8] O. Uckermann, W. Yao, T.A. Juratli, R. Galli, E. Leipnitz, M. Meinhardt, E. Koch, G. Schackert, G. Steiner, M. Kirsch, IDH1 mutation in human glioma induces chemical alterations that are amenable to optical Raman spectroscopy, Journal of Neuro-Oncology 139 (2018), https://doi.org/10.1007/s11060-018-2883-8.
[9] T. Sciortino, R. Secoli, E. D'amico, S. Moccia, M.C. Nibali, L. Gay, M. Rossi, N. Pecco, A. Castellano, E. De Momi, B. Fernandes, M. Riva, L. Bello, Raman spectroscopy and machine learning for idh genotyping of unprocessed glioma biopsies, Cancers (basel). 13 (2021), https://doi.org/10.3390/cancers13164196.
[10] Y. Zhou, C.H. Liu, B. Wu, C. Zhang, X. Yu, G. Cheng, H. Chen, S. Li, Q. Liang, M. Zhang, K. Zhu, L. Shi, R.R. Alfano, Invited Article: Molecular biomarkers characterization for human brain glioma grading using visible resonance Raman spectroscopy, APL Photonics 3 (2018), https://doi.org/10.1063/1.5036637.
[11] L.J. Livermore, M. Isabelle, I. Mac Bell, C. Scott, J. Walsby-Tickle, J. Gannon, P. Plaha, C. Vallance, O. Ansorge, Rapid intraoperative molecular genetic classification of gliomas using Raman spectroscopy, Neuro-Oncology Adv. 1 (2019), https://doi.org/10.1093/noajnl/vdz008.
[12] Y. Zhou, C.-H. Liu, B. Wu, X. Yu, G. Cheng, K. Zhu, K. Wang, C. Zhang, M. Zhao, R. Zong, L. Zhang, L. Shi, R.R. Alfano, Optical biopsy identification and grading of gliomas using label-free visible resonance Raman spectroscopy, Journal of Biomedical Optics 24 (2019), https://doi.org/10.1117/1.jbo.24.9.095001.
[13] M. Riva, T. Sciortino, R. Secoli, E. D'Amico, S. Moccia, B. Fernandes, M. Conti Nibali, L. Gay, M. Rossi, E. De Momi, L. Bello, Glioma biopsies Classification Using Raman Spectroscopy and Machine Learning Models on Fresh Tissue Samples, Cancers (basel) 13 (2021), https://doi.org/10.3390/cancers13051073.
[14] B. Broadbent, J. Tseng, R. Kast, T. Noh, M. Brusatori, S.N. Kalkanis, G.W. Auner, Shining light on neurosurgery diagnostics using Raman spectroscopy, Journal of Neuro-Oncology 130 (2016), https://doi.org/10.1007/s11060-016-2223-9.
[15] N. Iturrioz-Rodríguez, D. De Pasquale, P. Fiaschi, G. Ciofani, Discrimination of glioma patient-derived cells from healthy astrocytes by exploiting Raman spectroscopy, Spectrochim. Acta - Part A Mol. Biomol. Spectrosc. 269 (2022), https://doi.org/10.1016/j.saa.2021.120773.
[16] S. Koljenović, L.P. in. Choo-Smith, T.C.B. Schut, J.M. Kros, H.J. Van den Berge, G.J. Puppels,, Discriminating vital tumor from necrotic tissue in human glioblastoma tissue samples by Raman spectroscopy, Lab. Investig. 82 (2002), https://doi.org/10.1097/01.LAB.0000032545.96931.B8.
[17] J. Zhang, Y. Fan, M. He, X. Ma, Y. Song, M. Liu, J. Xu, Accuracy of Raman spectroscopy in differentiating brain tumor from normal brain tissue, Oncotarget. 8 (2017). 10.18632/oncotarget.15975.
[18] R.E. Kast, G.W. Auner, M.L. Rosenblum, T. Mikkelsen, S.M. Yurgelevic, A. Raghunathan, L.M. Poisson, S.N. Kalkanis, Raman molecular imaging of brain frozen tissue sections, Journal of Neuro-Oncology 120 (2014), https://doi.org/10.1007/s11060-014-1536-9.
[19] C. Krafft, S. Miljanic, S.B. Sobottka, G. Schackert, R. Salzer, Near infrared Raman spectroscopy to study the composition of human brain tissue and tumors, Opt. Infobase Conf. Pap. (2003), https://doi.org/10.1117/12.500469.
[20] J. Desroches, M. Jermyn, M. Pinto, F. Picot, M.A. Tremblay, S. Obaid, E. Marple, K. Urmey, D. Trudel, G. Soulez, M.C. Guiot, B.C. Wilson, K. Petrecca, F. Leblond, A new method using Raman spectroscopy for in vivo targeted brain cancer tissue biopsy, Scientific Reports 8 (2018), https://doi.org/10.1038/s41598-018-20233-3.
[21] Z. Jin, Q. Yue, W. Duan, A. Sui, B. Zhao, Y. Deng, Y. Zhai, Y. Zhang, T. Sun, G. P. Zhang, L. Han, Y. Mao, J. Yu, X.Y. Zhang, C. Li, Intelligent SERS Navigation System Guiding Brain Tumor Surgery by Intraoperatively Delineating the Metabolic Acidosis, Advancement of Science 9 (2022), https://doi.org/10.1002/advs.202104935.
[22] J. Sun, H. Fang, Z. Zhang, M. Chen, J. Tian, L. Chen, X. Zou, H. Yin, J. Yin, Detection of glioma by surface-enhanced Raman scattering spectra with optimized mathematical methods, Journal of Raman Specroscopy 50 (2019), https://doi.org/10.1002/jrs.5634.
[23] L. Zhou, J. Yang, X. Wang, G. Song, F. Lu, L. You, J. Li, Ag nanoparticles decorated Ag@ZrO2 composite nanospheres as highly active SERS substrates for quantitative detection of hexavalent chromium in waste water, Journal of Molecular Liquids 319 (2020), https://doi.org/10.1016/j.molliq.2020.114158.
[24] M. Yi, Y. Zhang, J. Xu, D. Deng, Z. Mao, X. Meng, X. Shi, B. Zhao, Surface-enhanced raman scattering activity of zro2 nanoparticles: Effect of tetragonal and monoclinic phases, Nanomaterials 11 (2021), https://doi.org/10.3390/nano11092162.
[25] X.Y. Wang, J. Yang, L. Zhou, G. Song, F. Lu, L.J. You, J.M. Li, Rapid and ultrasensitive surface enhanced Raman scattering detection of hexavalent chromium using magnetic Fe3O4/ZrO2/Ag composite microsphere substrates, Colloids Surfaces A Physicochem. Eng. Asp. 610 (2021), https://doi.org/10.1016/j.colsurfa.2020.125414.
[26] B.A. Hanson, ChemoSpec : An R Package for Chemometric Analysis of Spectroscopic Data and Chromatograms (Package version 2 . 0-2), Github.Com/Bryanhanson/. (2015).
[27] D.A. Whitaker, K. Hayes, A simple algorithm for despiking Raman spectra, Chemometrics and Intelligent Laborary Systems 179 (2018), https://doi.org/10.1016/j.chemolab.2018.06.009.
[28] X. Shen, L. Xu, S. Ye, R. Hu, L. Jin, H. Xu, W. Liu, Automatic baseline correction method for the open-path Fourier transform infrared spectra by using simple iterative averaging, Optics Express 26 (2018), https://doi.org/10.1364/oe.26.00a609.
[29] R.D. Purohit, S. Saha, A.K. Tyagi, Combustion synthesis of nanocrystalline ZrO2 powder: XRD, Raman spectroscopy and TEM studies, Mater. Sci. Eng. B Solid-State Mater. Adv. Technol. 130 (2006), https://doi.org/10.1016/j.mseb.2006.02.041.
[30] B. Varnholt, P. Oulevey, S. Luber, C. Kumara, A. Dass, T. Bürgi, Structural information on the Au-S interface of thiolate-protected gold clusters: A raman spectroscopy study, Journal of Physical Chemistry C 118 (2014), https://doi.org/10.1021/jp502453q.
[31] J.M. Estrela, A. Ortega, E. Obrador, Glutathione in cancer biology and therapy, Critical Reviews in Clinical Laboratory Sciences 43 (2006), https://doi.org/10.1080/10408360500523878.